Electronic reconstruction forming a C-2-symmetric Dirac semimetal in Ca3Ru2O7

npj | Quantum Materials

www.nature.com/npjquantmats

ARTICLE OPEN

Check for updates

Electronic reconstruction forming a C_2-symmetric Dirac semimetal in $Ca_3Ru_2O_7$

M. Horio[1]✉, Q. Wang[1], V. Granata[2,3], K. P. Kramer[1], Y. Sassa[4], S. Jöhr[1], D. Sutter[1], A. Bold[1], L. Das[1], Y. Xu[1], R. Frison[5], R. Fittipaldi[2,3], T. K. Kim[6], C. Cacho[6], J. E. Rault[7], P. Le Fèvre[7], F. Bertran[7], N. C. Plumb[8], M. Shi[8], A. Vecchione[2,3], M. H. Fischer[1] and J. Chang[1]✉

Electronic band structures in solids stem from a periodic potential reflecting the structure of either the crystal lattice or electronic order. In the stoichiometric ruthenate $Ca_3Ru_2O_7$, numerous Fermi surface-sensitive probes indicate a low-temperature electronic reconstruction. Yet, the causality and the reconstructed band structure remain unsolved. Here, we show by angle-resolved photoemission spectroscopy, how in $Ca_3Ru_2O_7$ a C_2-symmetric massive Dirac semimetal is realized through a Brillouin-zone preserving electronic reconstruction. This Dirac semimetal emerges in a two-stage transition upon cooling. The Dirac point and band velocities are consistent with constraints set by quantum oscillation, thermodynamic, and transport experiments, suggesting that the complete Fermi surface is resolved. The reconstructed structure—incompatible with translational-symmetry-breaking density waves—serves as an important test for band structure calculations of correlated electron systems.

npj Quantum Materials (2021)6:29; https://doi.org/10.1038/s41535-021-00328-3

INTRODUCTION

A Fermi-surface reconstruction refers to the sudden change of the electronic band structure as a function of a tuning parameter. As most electronic properties are governed by electrons in the vicinity of the Fermi level, a change of the Fermi-surface topology can have profound ramifications. Those reconstructions that are not obviously linked to a symmetry change of the crystal structure are of particular interest. Common triggers of Fermi-surface reconstructions are translational-symmetry breaking spin- or charge-density waves. Typically, this reduction of symmetry and the resulting folding of the Brillouin zone lead large Fermi-surface contours to split into smaller pockets. Once reconstructed, it is, however, often difficult to identify the Fermi surface structure. The high-temperature superconductor $YBa_2Cu_3O_{7-x}$ is a good example of this. In the underdoped regime, charge-density-wave order[1–3] clearly reconstructs the Fermi surface. Although quantum oscillations[4,5] and transport[6,7] experiments have revealed the existence of an electron pocket, the reconstructed Fermi-surface topology is, despite strong effort, still not clarified[8]. Another prominent example is the orthorhombic bilayer ruthenate $Ca_3Ru_2O_7$. An initial A-type antiferromagnetic (AFM) order setting in at $T_N = 56$ K[9] has no significant impact on the transport properties[10]. A spin reorientation from the orthorhombic *a*- to the *b*-axis direction[11,12] occurs at $T_{s1} = 48$ K. While this lattice-space-group preserving reorientation[9] naively might appear to be of minor consequence, the transition at $T_{s1} = 48$ K marks a dramatic electronic transformation.

Across this transformation, the Seebeck coefficient undergoes a sharp sign change taking large negative values below the transition temperature[13,14]. T_{s1} is also the onset of in-plane anisotropic transport properties[14]. Although transport and thermodynamic experiments provide information about Fermi surface area and electronic masses[15,16], the complete reconstructed Fermi surface has so far remained undetermined. Previously reported angle-resolved photoemission spectroscopy (ARPES) data have revealed the existence of a boomerang-shaped Fermi surface[17]. Obviously, a single pocket is insufficient to explain the observed ambipolar electronic properties[14]. Although a density-wave state has never been identified[12], a common assumption is that a translational-symmetry-breaking order reconstructs the Fermi surface into multiple sheets. However, as long as the complete Fermi surface and its orbital composition remain unidentified, so do the reconstructing mechanism.

Here, we provide by direct ARPES experiments the complete Fermi surface structure of $Ca_3Ru_2O_7$ across the electronic reconstruction. Above the reconstructing temperature, the low-energy electronic structure resembles that of a strongly correlated metal consistent with its orthorhombic crystal structure. The reconstructed Fermi surface by contrast consists of a small electron pocket formed by massive Dirac fermions along the short-axis orthorhombic zone boundary and a boomerang-like hole pocket in vicinity to the long-axis zone boundary. As the orthorhombic order parameter $|a-b|/(a+b)$ remains essentially unchanged across the reconstruction[9], the sudden emergence of such a dramatic Fermi surface anisotropy is unexpected. We furthermore demonstrate that the Fermi surface transformation appears in two steps. The anisotropic zone-boundary Fermi surfaces first appear below $T_{s1} = 48$ K and eventually the Dirac fermions settle into the low-temperature structure below $T_{s2} = 30$ K. Throughout this temperature evolution, no signature of Brillouin-zone folding is identified, excluding translational-symmetry breaking density-wave/orbital orders as the origin of the phase transition at $T_{s1} = 48$ K. We argue that the reconstructed

[1]Physik-Institut, Universität Zürich, Winterthurerstrasse 190, CH-8057 Zürich, Switzerland. [2]CNR-SPIN, I-84084 Fisciano, Salerno, Italy. [3]Dipartimento di Fisica 'E.R. Caianiello', Università di Salerno, I-84084 Fisciano, Salerno, Italy. [4]Department of Physics, Chalmers University of Technology, SE-412 96 Göteborg, Sweden. [5]Center for X-ray Analytics, Swiss Federal Laboratories for Materials Science and Technology (Empa), Überlandstrasse 129, CH-8600 Dübendorf, Switzerland. [6]Diamond Light Source, Harwell Campus, Didcot OX11 0DE, UK. [7]Synchrotron SOLEIL, Saint-Aubin-BP 48, F-91192 Gif sur Yvette, France. [8]Swiss Light Source, Paul Scherrer Institut, CH-5232 Villigen, Switzerland. ✉email: mhorio@issp.u-tokyo.ac.jp; johan.chang@physik.uzh.ch

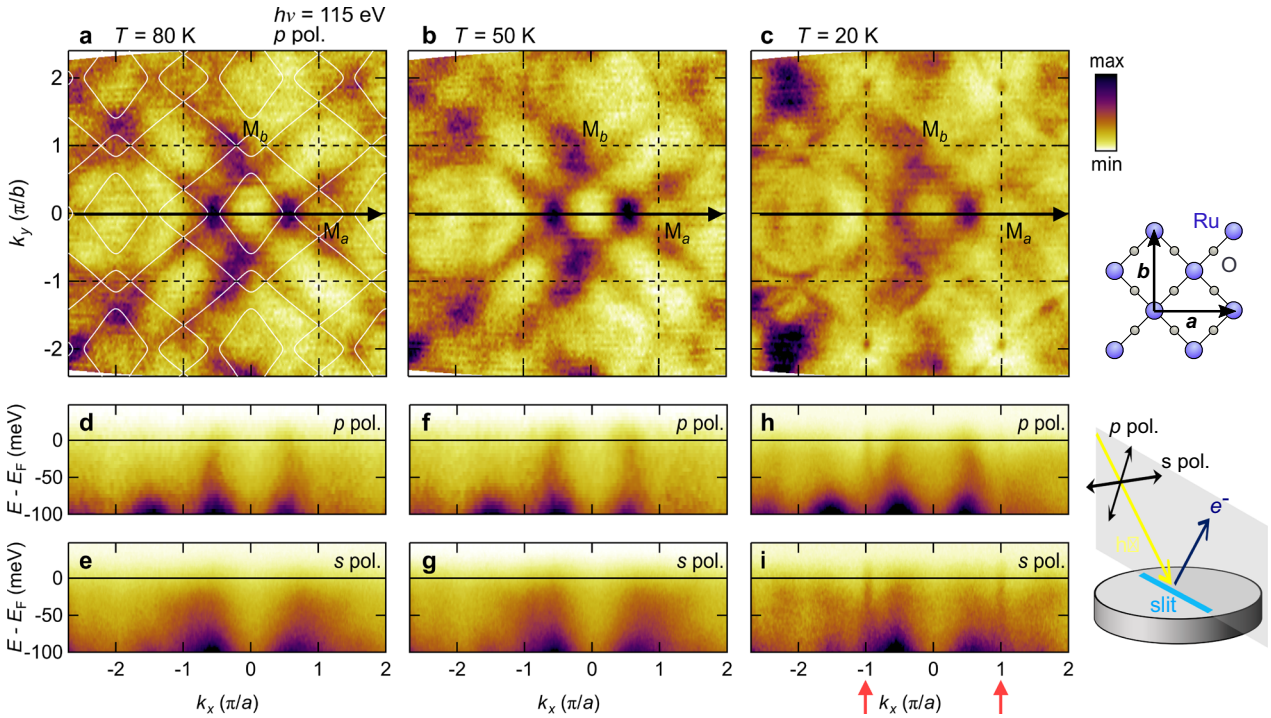

Fig. 1 Fermi-surface reconstruction in $Ca_3Ru_2O_7$. a–c Fermi surface maps taken at $T = 80$, 50, and 20 K, respectively. The photoelectron intensities -- displayed using a false color scheme—are integrated within $E_F \pm 20$ meV. White lines in **a** represent a tight-binding model (see Supplementary Note 1 and Supplementary Fig. S1) of the Fermi surface. Vertical and horizontal dashed lines indicate the orthorhombic zone boundaries. The orthorhombic *a* and *b* axes are indicated in top right inset. **d–i** Energy distribution maps along the Γ–M_a direction for incident light polarisations and temperatures as indicated. Red arrows mark the fast dispersing bands that emerge below $T_{s1} = 48$ K. The photoemission mirror plane along with incident light polarisation and the orientation of the electron analyser slit is shown in the bottom inset. With this setting, matrix elements for even-parity orbitals are expected to be suppressed in the *s*-polarisation channel.

Fermi surface should be understood from the d_{xz} and d_{yz} orbitals whereas the d_{xy} sector is not crossing the Fermi level in the reconstructed phase. The revelation of the complete Fermi surface reconstruction provides an ideal test-bed for ab-initio band structure calculations beyond density-functional-theory concepts.

RESULTS

High-temperature state

The Fermi surface and low-energy electronic structure of the $Ca_3Ru_2O_7$ normal state—above the Néel temperature $T_N = 56$ K—are presented in Fig. 1a, d, and e. The orthorhombic zone boundary is indicated by black dashed lines in Fig. 1a. All quasiparticle dispersions are broad irrespective of whether linear *p*- or *s*-polarised light is used. Part of the Fermi surface consists of straight sectors running diagonally through the orthorhombic Brillouin zone. This quasi-one-dimensional structure remains essentially unchanged across the Néel transition at $T_N = 56$ K [see Fig. 1b, f, and g]. Furthermore, the orthorhombic zone boundary points $M_a = (\pm\pi/a, 0)$ and $M_b = (0, \pm\pi/b)$ are virtually indistinguishable (See also Supplementary Fig. S1).

Fermi surface anisotropy

Across the structural transition at $T_{s1} = 48$ K, however, the electronic structure undergoes a dramatic reconstruction. This is evidenced by the emergence of a fast dispersing band and a tiny Fermi surface around M_a—see Fig. 1c, h, and i. Remarkably, this small Fermi surface sheet is absent at M_b. Instead, as previously reported[17], boomerang-like Fermi surface sheets are found around the M_b point. Therefore, in contrast to $T > T_{s1}$, the low-temperature structure appears highly anisotropic featuring different Fermi surface topology around M_a and M_b. This Fermi surface reconstruction appears without change of the crystal lattice space group and with minute (~1%) reduction of the orthorhombic order parameter[9].

To exclude the possibility that this C_2 symmetry is an artefact of photoionization-matrix-element effects, we follow a standard measurement protocol[18,19]. That is to carry out Fermi surface mappings with azimuthal angles differing from each other by 90° [see Fig. 2a, b]. In situ azimuthal rotation implies that the Fermi surface maps in Fig. 2a, b are from the same surface. Here, $k_{\parallel}$ ($k_{\perp}$) on the horizontal (vertical) axis represents the momentum parallel (perpendicular) to the electron-analyser slit. The electronic structure with a tiny Fermi pocket around the M_a point and boomerang-like features near M_b tracks the azimuthal rotation—see Fig. 2a–d. The C_2-symmetric electronic structure is also revealed by the band dispersions. Along the M_a–Γ and M_b–Γ directions, the band curvature around M_a and M_b are clearly different [Fig. 2e, g]. An electron pocket is formed around M_a whereas two hole-like pockets are found on each side of M_b. In a similar fashion, dispersions along the M_a–X and M_b–X directions are inequivalent [Fig. 2f, h]. Electron-like band curvature is found around M_a whereas no Fermi-level crossing is observed along M_b–X. These results exclude matrix-element effects as the source of the observed anisotropy.

Two-stage Fermi surface reconstruction

Tracking the temperature dependence of the band structure reveals two electronic temperature scales. The electronic band structure along M_a–Γ and M_b–Γ is shown for temperatures going from 16 to 50 K. Above $T_{s1} = 48$ K [Fig. 3e, j and 1], all bands appear with broad line-shapes. Once cooled below T_{s1}, well-defined bands around the M_a and M_b points emerge [see Fig. 3d, i, and k]. The appearance of another electron-like band around the Γ point is

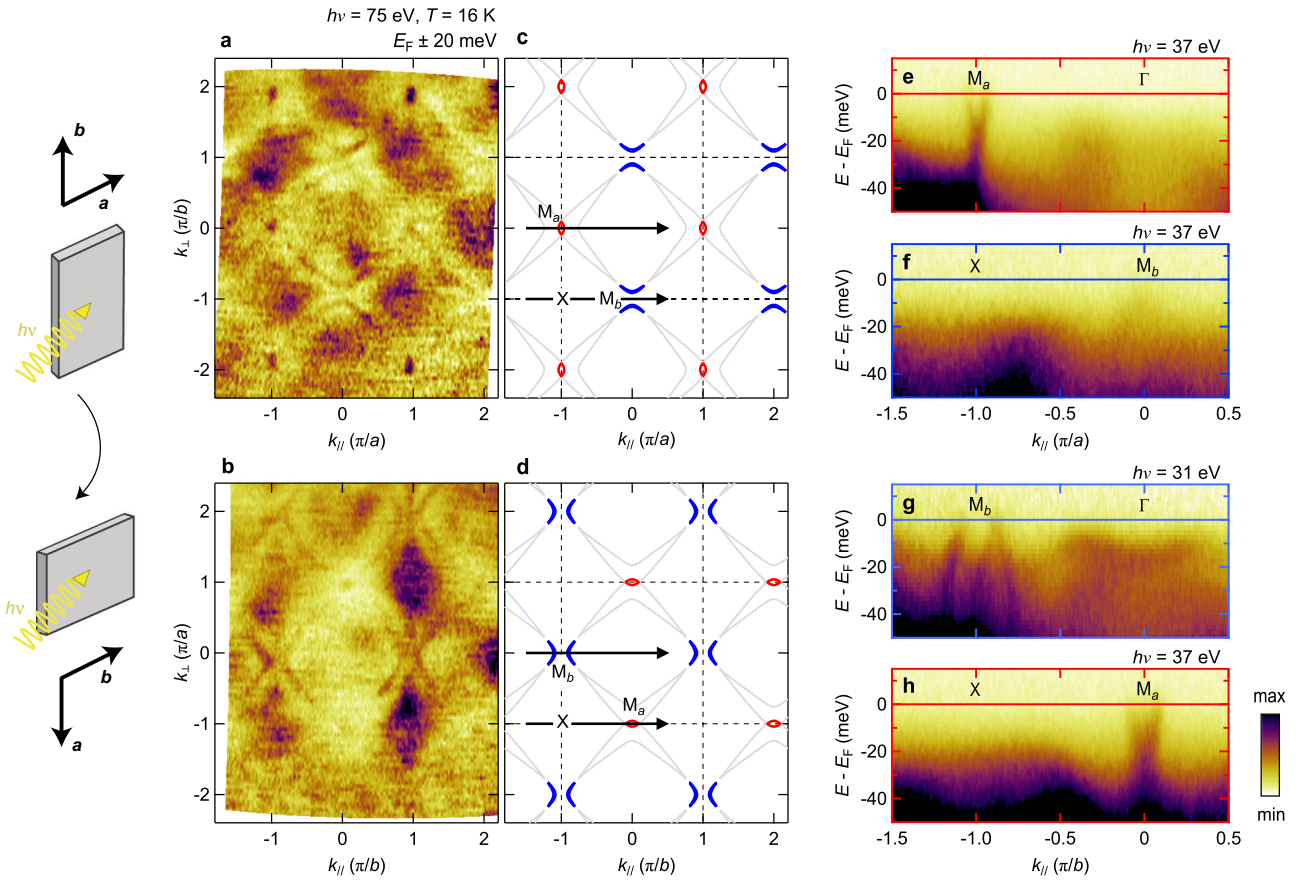

Fig. 2 Breaking of fourfold rotational symmetry. a, **b** Fermi surface maps recorded at $T = 16$ K ($h\nu = 75$ eV) for two sample azimuthal angles that are 90° apart as indicated in the schematics. The azimuthal angle rotation was operated in situ and hence the sample surface is identical. $k_{\parallel}$ ($k_{\perp}$) represents momentum parallel (perpendicular) to the electron-analyser slit. The spectral intensity was integrated within $E_F \pm 20$ meV, washing-out spectral gaps within the integration window. **c**, **d** Fermi surfaces from the tight-binding model (see Supplementary note 1). The sheets not observed in the experiment are indicated in grey. **e**–**h** Energy distribution maps along M_a–Γ, X–M_b, M_b–Γ, and X–M_a as shown in **c** and **d**. The energy distribution maps were recorded at $h\nu = 37$ eV except for **g** where $h\nu = 31$ eV incident light was selected to optimise the photoelectron matrix element. Systematic photon-energy dependence between 30 and 40 eV is presented in Supplementary Figs. S2 and S3. The band structure along with M_a–Γ (X–M_a) and M_b–Γ (X–M_b) is inequivalent.

accompanied by a gap Δ opening below T_{s1} [see Fig. 3g–i and Supplementary Fig. S4]. The band structures around M_a and M_b are inequivalent not only in terms of curvature but also in terms of temperature dependence. The M_a–Γ band dispersion is temperature-dependent whereas the corresponding structure around M_b is virtually insensitive to temperature. Examining the M_a–Γ direction, two inequivalent bands with different Fermi momenta are observed for $30 < T < 48$ K whereas only a single set of bands is resolved for $T < 30$ K—see Fig. 3. The two bands around M_a display asymmetric matrix elements. Momentum distribution curves (MDCs) at E_F and $30 < T < 48$ K are therefore not symmetric around M_a. Upon cooling below 30 K, the single electron pocket around M_a displays symmetric Fermi momenta k_F despite the asymmetric matrix elements. To illustrate the transition between the two- and single-band situation, we define Δk_F as the reciprocal-space distance between the two MDC-intensity maxima. Across $T_{s2} = 30$ K, Δk_F drops by a factor of two. This observation is independent of incident-light polarisation (see Supplementary Figs. S5 and S6). On the other hand, the gap Δ evolves smoothly across T_{s2} [see Fig. 3g–i and Supplementary Fig. S4], suggesting that the states around Γ are not involved in this transition. Although $T_{s2} = 30$ K remains to be identified as a thermodynamic temperature scale, it does coincide with the onset of a strong negative Nernst effect response[14] [see Fig. 3l]. We also notice that the reduction of Δk_F below T_{s2} is consistent with an increasing Nernst effect $\nu/T \propto \mu/\varepsilon_F$ where μ is the electron mobility and ε_F the Fermi energy[20], as lower Δk_F implies a smaller Fermi energy. The low-temperature Fermi surface thus emerges as a result of two reconstructions. First below $T_{s1} = 48$ K, a fast dispersing band appears around M_a and M_b with a gap opening for other bands. Next, the band dispersion along the M_a–Γ direction undergoes a second transformation across $T_{s2} = 30$ K.

Low-temperature electronic structure

With the exception of the features around the M_a and M_b points, all other bands are not crossing the Fermi level for $T < T_{s2}$—see Fig. 2e–h. Around the M_b point, two hole-like bands—forming an M-shaped structure—are found [Fig. 2g]. While the hole-like band touches E_F along the M_b–Γ direction [Fig. 2g], the band top sinks below E_F upon moving away from it by ~ $0.1\pi/b$. (See Supplementary Fig. S7) consistent with a previous report[17]. The boomerang-like feature thus forms a closed hole-like Fermi surface. Around the M_a point, the electron-like Fermi surface pocket is revealed by a high-resolution map in Fig. 4(a). The electron pocket is elliptical with $k_F^a = 0.04\pi/a$ and $k_F^b = 0.07\pi/b$ along the M_a–Γ and M_a–X directions, respectively. The Fermi surface area $A_{FS} = \pi k_F^a k_F^b$ corresponds to 0.23% of the orthorhombic Brillouin zone. Inspecting the band dispersion along the M_a–Γ direction reveals a Dirac-cone structure with the Dirac point placed about $E_D = 15$ meV below E_F [Fig. 4b]. The two-peak MDC profile found at E_F merges into a single peak at E_D and then

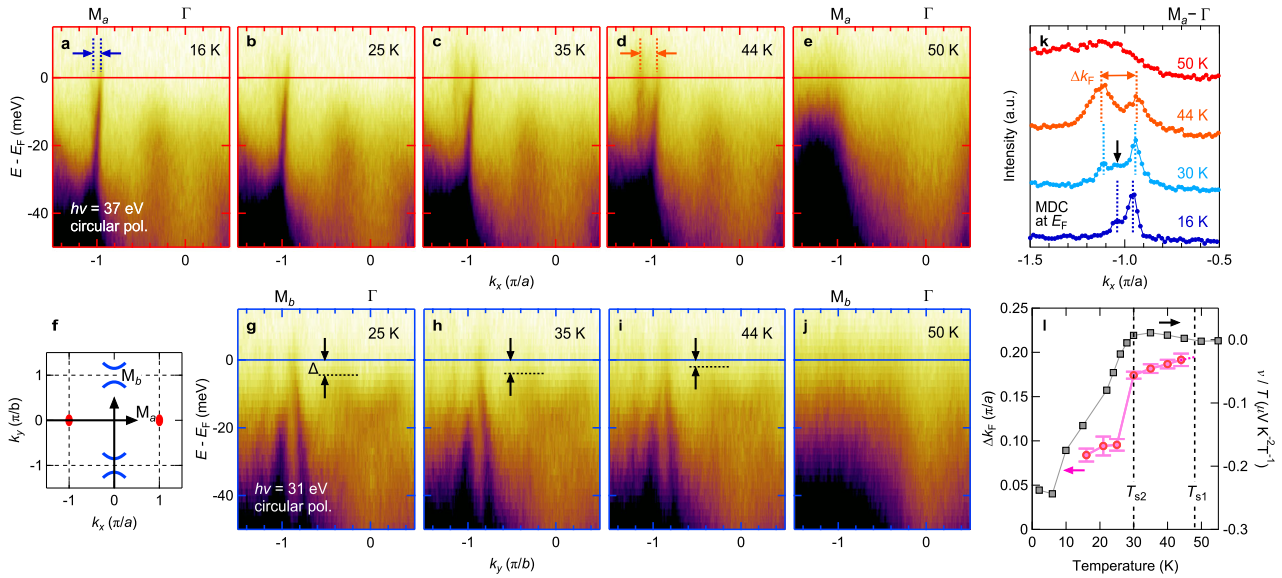

Fig. 3 Two-stage temperature evolution of the band structure. a–j Energy distribution maps along M_a--Γ (top panels) and M_b--Γ (bottom panels) for temperatures as indicated. The gap Δ of the electron pocket around Γ is indicated in **g–i**. For detailed analysis, see Supplementary Fig. S4. **f** Schematics of the Fermi surface and the high-symmetry cuts used in **a–e** and **g–j**. **k** MDCs at E_F (integrated within ± 3 meV) for temperatures as indicated. Vertical dashed lines define MDC peak maxima. A clear difference in the peak separation, Δk_F, is found across 30 K. At 30 K, a three-peak structure is found and indicated by the black arrow and the two dashed lines. **l** Δk_F plotted as a function of temperature. The error bars represent 3σ of the fitting with σ being the standard deviation. For comparison, the Nernst coefficient ν[14] is plotted as ν/T versus T. Both experiments suggest an electronic transformation across $T = 30$ K.

splits again below E_D [see Fig. 4c]. This MDC analysis estimates a linear Fermi velocity of $v_F^a = 0.62$ eVÅ (95 km/s) and $v_F^b = 0.37$ eVÅ (57 km/s) (see Supplementary Fig. S8). Our results thus suggest that $Ca_3Ru_2O_7$ at low temperatures is a highly anisotropic Dirac semimetal.

DISCUSSION

The low-temperature resistivity anisotropy in $Ca_3Ru_2O_7$, is as large as $\rho_c/\rho_{ab} \sim 1000$[10]. It is, therefore, reasonable to consider the Fermi surface to be two-dimensional. This implies that quantum oscillation and ARPES experiments are directly comparable. Onsager's relation[5] links directly Fermi surface areas to quantum oscillation frequencies $F = \Phi_0 A_{FS}/(2\pi^2)$ where Φ_0 is the flux quantum. The low-temperature electron pocket around M_a corresponds to $F = 34$ T in agreement with observed quantum oscillation frequencies 28–43 T[14–16]. The hole-like boomerang structure comprises a Fermi surface area that is too small to be quantified accurately by our ARPES experiments. However, it should produce a low-frequency quantum oscillation. Indeed, a frequency corresponding to 0.07% of the Brillouin zone or about 1/3 of the electron pocket has been reported[15]. It is therefore conceivable that the electron and hole Fermi pockets reported here are those responsible for the quantum oscillations. Our ARPES work unveils the band curvature and position of these pockets within the Brillouin zone.

Combining ARPES and quantum oscillation experiments allows direct comparison of the effective electronic mass $m^* = \frac{\hbar^2}{2\pi}\frac{\partial A_{FS}}{\partial \varepsilon}$[21,22] on the electron pocket. Lifshitz–Kosevich analysis of the ~35 T quantum-oscillation frequency yield $m_e^* = 0.6 m_e$[16], where m_e is the free electron mass. Assuming a parabolic band dispersion $m_e^* = \hbar^2 k_F^a k_F^b / 2\varepsilon_F$ where $\varepsilon_F = 15$ meV is the Fermi energy, the effective mass $m_e^* = 0.25 m_e$ is significantly lower than that inferred from quantum-oscillation experiments. A linear band dispersion $E_k = v_F k$ provides a much better agreement $m_e^* = \varepsilon_F / v_F^a v_F^b = \hbar^2 k_F^a k_F^b / \varepsilon_F = 0.49 m_e$. This fact reinforces the interpretation of Dirac fermions around M_a. The boomerang band along Γ–M_b has comparable Fermi velocity to that of the electron pocket along Γ–M_a. Estimation of the Fermi energy from linear extrapolation of the M-shaped band dispersion yields $\varepsilon_F \sim 5$ meV, which is about three times smaller than that obtained for the electron pocket. As the hole pocket area—according to quantum-oscillation measurements[15]—is also about three times smaller than the electron sheet, we estimate the hole-like carriers to have a comparable effective mass of $m_h^* = 0.49 m_e$. With two hole and one electron pocket per Brillouin zone, a Sommerfeld constant of $\gamma \approx 2.1$ mJ mol^{-1} K^{-2} is found, with mol refering to one formula unit. Here, we assumed two-dimensional band dispersions without bi-layer splitting and used the two-dimensional expression $\gamma = \pi N_A k_B^2 ab / 3\hbar^2 \sum_i m_i$[16], where N_A is the Avogadro constant, k_B is the Boltzmann constant, $\hbar$ is the reduced Planck constant, and m_i is the effective mass. In addition, spin polarisation within the RuO_2 plane was employed to treat the A-type AFM order. As our estimate is in reasonable agreement with the value $\gamma \approx 2.8$–3.4 mJ mol^{-1} K^{-2}) obtained by specific heat experiments[10,16], we conclude that our experiments reveal the entire bulk Fermi surface.

The two-stage transformation of the electronic structure has a clear impact on all transport coefficients. A remarkable increase of in- and out-of-plane resistivity appears across $T_{s1} = 48$ K[10,16]. Simultaneously, the Seebeck coefficient changes sign going from weak positive to large negative values across T_{s1}[14]. Although less sharp, the Hall coefficient also changes sign (from positive to negative) across T_{s1}. While the Hall coefficient takes increasingly large negative values[14,23], the Seebeck coefficient displays a complicated temperature dependence that in addition is different along the a and b directions[14]. This temperature dependence is a typical signature of ambipolar transport behaviour, where both electron- and hole-like carriers are contributing[24]. Furthermore, the low-temperature Hall coefficient R_H that (in different studies) ranges from -0.5×10^{-7} m^3 C^{-1} to -1.4×10^{-7} m^3 C^{-1} [14,16,23] cannot be explained by the electron pocket that alone should generate $R_H = -1/(n_e e) = -8.0 \times 10^{-7}$ m^3 C^{-1}. Using the combined ARPES and quantum-oscillation knowledge that $n_e = 7.8 \times 10^{18}$ cm^{-3} and $n_h \approx 2 \times n_e/3$, a two band model[25] yields $R_H = (2a^2/3 - 1)/(n_e e)$

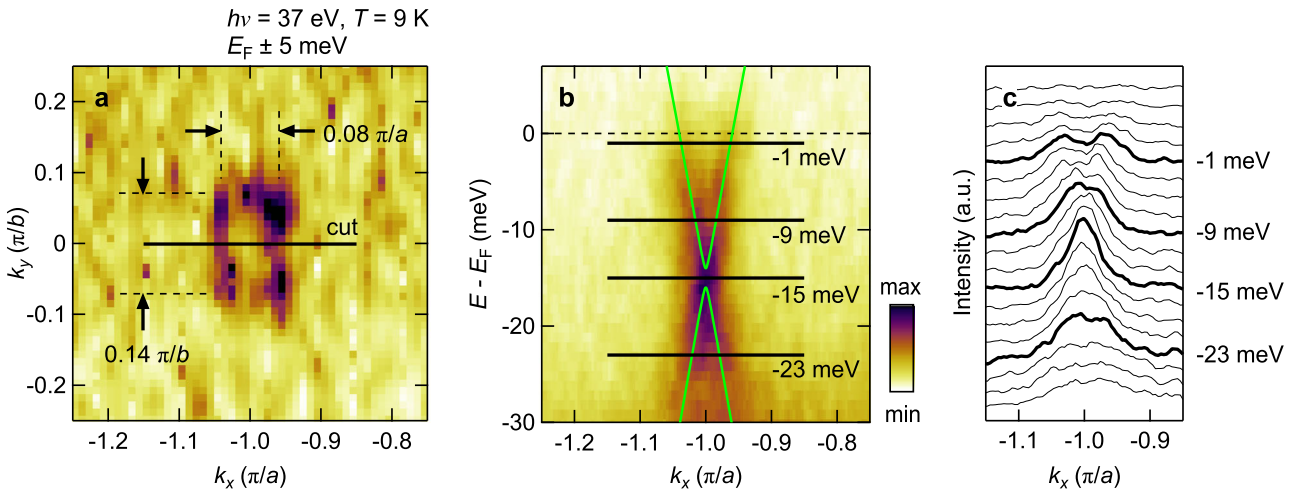

Fig. 4 Dirac cone structure in $Ca_3Ru_2O_7$. a High-resolution Fermi surface map around the M_a point. **b** Energy distribution map along the M_a–Γ direction evidencing a Dirac cone structure. Crystal/magnetic symmetry imposes a finite mass as illustrated by green dispersions reproduced by the tight-binding model (see Supplementary Note 1). **c** MDCs, extracted from **b** at binding energies as indicated.

$(2a/3+1)^2$ where $a=\mu_h/\mu_e$ is the mobility ratio between electrons and holes. The exact experimental values of $R_H(T=0)$ imply that $\mu_h \approx 0.9$–$1.1 \times \mu_e$ and $\mu_e \approx |R_H|/\rho_{xx} = 0.1\ T^{-1}$. We thus infer that in the $T \to 0$ limit electron- and hole-like carriers have comparable mobility that in turn generate the ambipolar transport properties.

Having established the existence of small electron pockets with linear dispersion around the M_a point, a question arises whether these excitations are massless Dirac fermions or whether they possess a finite mass at M_a. While the question cannot be definitively answered from the experimental data due to the finite energy resolution, we discuss here implications from the crystal symmetry. $Ca_3Ru_2O_7$ has the space group $Bb2_1m$ (No. 36)[9]. For our purpose, it is sufficient to focus on a single bi-layer. The point group of such a bi-layer is C_{2v} with a mirror plane between the two layers, as well as a glide plane perpendicular to the mirror and a two-fold screw axis along the crystalline b axis (the longer in-plane axis). Together with time-reversal symmetry (TRS) in the paramagnetic state, this imposes a Kramer's degeneracy along M_b–X in the Brillouin zone. Furthermore, TRS imposes Kramer's pairs at the M_a and Γ point.

When TRS is broken in the A-type AFM phase[11], the generating point group of the bi-layer is reduced to C_{2v} (C_s) for the AFM-a phase and C_{2v} (C_2) for the AFM-b phase. Here, the notation $\mathcal{G}$ ($\mathcal{G}'$) denotes the generating point group $\mathcal{G}$ with $\mathcal{G}'$ the subgroup of elements that do not have to be combined with TRS. While Kramer's degeneracy is preserved along with M_b–X, the one at the M_a and Γ point is lifted. The Dirac fermions at M_a thus possess a finite mass, in other words, the bands hybridise as schematically illustrated in Fig. 4b.

Finally, we can reproduce key features of the low-temperature semimetallic band structure employing a tight-binding model of the Ru t_{2g} orbitals (see Supplementary Note 1, Supplementary Figs. S1 and S9). We restrict our model to the Ru d_{xz} and d_{yz} orbitals in an effective single-layer model, for two reasons. Firstly, the "one-dimensional" nature of the high-temperature ($T > 48$ K) Fermi surface resembles the d_{xz}, d_{yz} dominated α and β bands of other ruthenates[26,27]. Secondly, the matrix-element effect of the electron pocket around M_a is incompatible with the expectation of selection rules for the d_{xy} orbital character [see Fig. 1h, i]. Our simple model faithfully reproduces the Fermi surface in the normal state [see Fig. 1a and Supplementary Fig. S1]. Importantly, a rigid band shift in the d_{xz}/d_{yz} sector, as expected due to the c-axis compression at T_{s1}[9], yields elliptical electron pockets with linear dispersion around the M_a point and a hole-like boomerang structure around the M_b point [Fig. 2c, d]. This d_{xz}/d_{yz} band shift implies a change of orbital polarisation to respect the global charge balance. Finally, the Brillouin-zone folding due to the screw-axis opens a gap around the M_a Dirac point [see green lines Fig. 4b]. Due to the small gap size and Dirac point distance from the Fermi level, this gap is irrelevant for transport and thermodynamic measurements. While our tight-binding model based on the Ru t_{2g} orbitals is too simplistic to capture all the features and does not include the actual electronic instability, it reproduces the most salient features of both the high- and low-temperature dispersions. We thus conclude that the low-temperature low-energy band structure stems primarily from the d_{xz} and d_{yz} Ru orbitals.

A fundamental remaining question links to the triggering mechanism that induces the Dirac semimetal. Specific heat suggests that the phase transition at T_{s1} involves a large entropy change[10] and unlike other layered ruthenates, the ground state is a low density-of-state semimetal. It has been argued that the reorientation of the magnetic moments alone can not account for this large entropy change. Upon cooling, an energy gain of the system is manifested by an electronic reconstruction that opens a gap leaving only small Fermi surface pockets around the zone boundaries. Most likely, this Fermi surface reconstruction is triggered by an electronic mechanism. Density-wave orders breaking translation symmetry are, however, excluded since the reconstruction preserves the original Brillouin-zone boundaries. This leads us to speculate alternative scenarios, with electron correlations likely involved in some way. If so, the situation resembles that of the single-layer counterpart Ca_2RuO_4 where the instability toward a Mott-insulating state triggers a large c-axis lattice contraction[28–30]. Indeed, a c-axis lattice contraction is found across the first (48 K) transition though this effect is much less pronounced in $Ca_3Ru_2O_7$[9]. Alternatively, it has been proposed that $Ca_3Ru_2O_7$ hosts magnetic anapole order[31,32]. This would connect $Ca_3Ru_2O_7$ with hidden order problems in the sense that it is very difficult to demonstrate experimentally.

Note added after completion of this work: A recent complementary ARPES study[33] conducted at $T \geqq 30$ K suggested using DFT calculations including Rashba-type spin-orbit coupling that the electronic reconstruction across $T = 48$ K can be understood from the magnetic-moment reorientation alone without the need for additional hidden order.

METHODS

Sample characterisation

High-quality single crystals of $Ca_3Ru_2O_7$ were grown by floating zone technique[10]. The electronic transition at $T_{s1} = 48$ K was checked by thermopower measurements (see Supplementary Fig. S10) and found in agreement with existing literatures[13,14]. Detwinning of orthorhombic domains was achieved with a thermo-mechanical device[34] and monitored by polarised light microscopy. The resulting monodomain constitutes 99% (or more) of the sample volume according to X-ray diffraction measurements (see Supplementary Fig. S10).

ARPES experiments

ARPES experiments were carried out at the SIS[35], CASSIOPEE (https://www.synchrotron-soleil.fr/en/beamlines/cassiopee), and I05[36] beamlines of the Swiss Light Source, SOLEIL synchrotron, and Diamond Light Source, respectively. Pristine surfaces were obtained by top-post cleaving at $T > T_{s1}$ (80 K). Incident photons $h\nu = 31-115$ eV, providing high in-plane and modest out-of-plane[22] momentum resolution, were used for this study. Consistent results were obtained on different crystals and upon cooling and heating through the critical temperature $T_{s1} = 48$ K below which the electronic structure is reconstructed. ARPES data are presented using orthorhombic notation with lattice parameters $a = 5.37$ Å and $b = 5.54$ Å.

DATA AVAILABILITY

The data that support the findings of this study are available from the corresponding author upon reasonable request.

Received: 24 October 2020; Accepted: 23 February 2021;
Published online: 19 March 2021

REFERENCES

1. Wu, T. et al. Magnetic-field-induced charge-stripe order in the high-temperature superconductor $YBa_2Cu_3O_y$. *Nature* **477**, 191–194 (2011).
2. Ghiringhelli, G. et al. Long-range incommensurate charge fluctuations in (Y,Nd) $Ba_2Cu_3O_{6+x}$. *Science* **337**, 821–825 (2012).
3. Chang, J. et al. Direct observation of competition between superconductivity and charge density wave order in $YBa_2Cu_3O_y$. *Nat. Phys.* **8**, 871–876 (2012).
4. Doiron-Leyraud, N. et al. Quantum oscillations and the Fermi surface in an underdoped high-T_c superconductor. *Nature* **447**, 565–568 (2007).
5. Sebastian, S. E. & Proust, C. Quantum oscillations in hole-doped cuprates. *Annu. Rev. Condens. Matter Phys.* **6**, 411–430 (2015).
6. LeBoeuf, D. et al. Electron pockets in the Fermi surface of hole-doped high-T_c superconductors. *Nature* **450**, 533–536 (2007).
7. Chang, J. et al. Nernst and Seebeck coefficients of the cuprate superconductor $YBa_2Cu_3O_{6.67}$: a study of Fermi surface reconstruction. *Phys. Rev. Lett.* **104**, 057005 (2010).
8. Hossain, M. A. et al. In situ doping control of the surface of high-temperature superconductors. *Nat. Phys.* **4**, 527–531 (2008).
9. Yoshida, Y. et al. Crystal and magnetic structure of $Ca_3Ru_2O_7$. *Phys. Rev. B* **72**, 054412 (2005).
10. Yoshida, Y. et al. Quasi-two-dimensional metallic ground state of $Ca_3Ru_2O_7$. *Phys. Rev. B* **69**, 220411(R) (2004).
11. Bao, W. et al. Spin valve effect and magnetoresistivity in single crystalline $Ca_3Ru_2O_7$. *Phys. Rev. Lett.* **100**, 247203 (2008).
12. Bohnenbuck, B. et al. Magnetic structure and orbital state of $Ca_3Ru_2O_7$ investigated by resonant x-ray diffraction. *Phys. Rev. B* **77**, 224412 (2008).
13. Iwata, K. et al. Thermopower of double-layered ruthenate $Ca_3Ru_2O_7$. *J. Magn. Magn. Mater.* **310**, 1125–1127 (2007).
14. Xing, H. et al. Existence of electron and hole pockets and partial gap opening in the correlated semimetal $Ca_3Ru_2O_7$. *Phys. Rev. B* **97**, 041113(R) (2018).
15. Cao, G. et al. Quantum oscillations, colossal magnetoresistance, and the magnetoelastic interaction in bilayered $Ca_3Ru_2O_7$. *Phys. Rev. B* **67**, 184405 (2003).
16. Kikugawa, N. et al. $Ca_3Ru_2O_7$: density wave formation and quantum oscillations in the hall resistivity. *J. Phys. Soc. Jpn.* **79**, 024704 (2010).
17. Baumberger, F. et al. Nested Fermi surface and electronic instability in $Ca_3Ru_2O_7$. *Phys. Rev. Lett.* **96**, 107601 (2006).
18. Yi, M. et al. Symmetry-breaking orbital anisotropy observed for detwinned $Ba(Fe_{1-x}Co_x)_2As_2$ above the spin density wave transition. *Proc. Natl Acad. Sci.* **108**, 6878–6883 (2011).
19. Watson, M. D. et al. Electronic anisotropies revealed by detwinned angle-resolved photo-emission spectroscopy measurements of FeSe. *N. J. Phys.* **19**, 103021 (2017).
20. Behnia, K. The Nernst effect and the boundaries of the Fermi liquid picture. *J. Phys. Condens. Matter* **21**, 113101 (2009).
21. Rourke, P. M. C. et al. A detailed de Haas van Alphen effect study of the overdoped cuprate $Tl_2Ba_2CuO_{6+\delta}$. *N. J. Phys.* **12**, 105009 (2010).
22. Horio, M. et al. Three-dimensional Fermi surface of overdoped La-based cuprates. *Phys. Rev. Lett.* **121**, 077004 (2018).
23. Yoshida, Y., Ikeda, S.-I. & Shirakawa, N. Hall effect in $Ca_3Ru_2O_7$. *J. Phys. Soc. Jpn.* **76**, 085002 (2007).
24. Bel, R., Behnia, K. & Berger, H. Ambipolar Nernst effect in $NbSe_2$. *Phys. Rev. Lett.* **91**, 066602 (2003).
25. Rourke, P. M. C. et al. Fermi-surface reconstruction and two-carrier model for the Hall effect in $YBa_2Cu_4O_8$. *Phys. Rev. B* **82**, 020514(R) (2010).
26. Damascelli, A. et al. Fermi surface, surface states, and surface reconstruction in Sr_2RuO_4. *Phys. Rev. Lett.* **85**, 5194 (2000).
27. Tamai, A. et al. Fermi surface and van Hove singularities in the itinerant metamagnet $Sr_3Ru_2O_7$. *Phys. Rev. Lett.* **101**, 026407 (2008).
28. Nakatsuji, S. & Maeno, Y. Quasi-two-dimensional Mott transition system $Ca_{2-x}Sr_xRuO_4$. *Phys. Rev. Lett.* **84**, 2666–2669 (2000).
29. Friedt, O. et al. Structural and magnetic aspects of the metal-insulator transition in $Ca_{2-x}Sr_xRuO_4$. *Phys. Rev. B* **63**, 174432 (2001).
30. Sutter, D. et al. Hallmarks of Hunds coupling in the Mott insulator Ca_2RuO_4. *Nat. Commun.* **8**, 15176 (2017).
31. Thöle, F. & Spaldin, N. A. Magnetoelectric multipoles in metals. *Philos. Trans. R. Soc. A* **376**, 20170450 (2018).
32. Lovesey, S. W., Khalyavin, D. D. & van der Laan, G. Magnetic multipoles in a ruthenate $Ca_3Ru_2O_7$. *Phys. Rev. B* **99**, 134444 (2019).
33. Marković, I. et al. Electronically driven spin-reorientation transition of the correlated polar metal $Ca_3Ru_2O_7$. *Proc. Natl Acad. Sci.* **117**, 15524–15529 (2020).
34. Burkhardt, E., Ye, Z.-G. & Schmid, H. Low and high temperature uniaxial stress devices for the study of ferroelastic crystals. *Rev. Sci. Instrum.* **66**, 3888–3893 (1995).
35. Flechsig, U., Patthey, L. & Schmidt, T. Performance measurements at the SLS spectroscopy beamline. *AIP Conf. Proc.* **705**, 316–319 (2004).
36. Hoesch, M. et al. A facility for the analysis of the electronic structures of solids and their surfaces by synchrotron radiation photoelectron spectroscopy. *Rev. Sci. Instrum.* **88**, 013106 (2017).

ACKNOWLEDGEMENTS

We thank M. Hoesch for fruitful discussions. M.H., Q.W., K.P.K., D.S., Y.X., and J.C. acknowledge support by the Swiss National Science Foundation. Y.S. is funded by the Swedish Research Council (VR) with a Starting Grant (Dnr. 2017-05078) and thanks Chalmers Areas of Advance-Materials Science. ARPES measurements were carried out at the SIS, CASSIOPEE, and I05 beamlines of the Swiss Light Source, SOLEIL synchrotron, and Diamond Light Source, respectively. We acknowledge Diamond Light Source for time at beamline I05 under proposal SI20259.

AUTHOR CONTRIBUTIONS

V.G., R.Fi., and A.V. grew and prepared single crystals. L.D. and Y.X. performed thermopower measurements. S.J. and M.H. detwinned single crystals. M.H., Q.W., S.J., and R.Fr. carried out x-ray and Laue diffraction measurements. M.H., Q.W., K.P.K., Y.S., D.S., A.B., and J.C. prepared and carried out the ARPES experiment with the assistance of T.K.K., C.C., J.E.R., P.L.F., F.B., N.C.P., and M.S. M.H. analyzed the ARPES data. M.H., M. H.F., and J.C. developed the tight-binding model. M.H., D.S., and J.C. conceived the project. All authors contributed to the manuscript.

COMPETING INTERESTS

The authors declare no competing interests.

ADDITIONAL INFORMATION

Supplementary information The online version contains supplementary material available at https://doi.org/10.1038/s41535-021-00328-3.

Correspondence and requests for materials should be addressed to M.H. or J.C.

Reprints and permission information is available at http://www.nature.com/reprints